Detection and characterization of optical inhomogeneities with diffuse photon density waves: a signal-to-noise analysis

D. A. Boas, M. A. O'Leary, B. Chance, and A. G. Yodh

Diffusing photons provide information about the optical properties of turbid media. In biological tissues these optical properties may be correlated to physiological parameters, enabling one to probe effectively the physiological states of tissue for abnormalities such as tumors and hemorrhages. We show that positional uncertainty in the source and detector lead to significant random errors that degrade the optical information available from diffusing photons. We investigate the limits for the detection, localization, and characterization of optical inhomogeneities by using diffusing photons as a probe. Although detection is sufficient for tumor screening, full characterization of the optical properties is desirable for specification of the tumor. Our findings in model breast systems with realistic signal-to-noise ratios indicate that tumors as small as 0.3 cm in diameter can be unambiguously detected; however, simultaneous determination of tumor size and optical properties is possible only if its diameter is of the order of 1.0 cm or larger. On the other hand, if *a priori* information about the size (optical properties) is available, then the optical properties (size) of tumors as small as 0.3 cm in diameter can be determined. © 1997 Optical Society of America

1. Introduction

The potential to acquire information noninvasively about tissue optical properties offers exciting possibilities for medical imaging. For this reason, the diffusion of near-infrared photons in turbid media has been the focus of substantial recent research.[1–4] Currently, pulse-time,[4–6] amplitude-modulated,[3,7–9] and continuous-wave sources of light[10–12] are used to probe turbid media for optical anomalies such as tumors and hematomas. At this stage it is desirable to establish fundamental limits for the detection and characterization of optical inhomogeneities in order to assess the degree with which diffusing photons can be effectively used to provide physiological information about tissues. Furthermore, an understanding

of these limiting factors will lead to the optimization of medical optical imaging prototypes.

Light does not travel ballistically through turbid media, but instead experiences many scattering events before its absorption or transmission through boundaries. For many biological tissues, the absorption length for near-infrared light is much longer than the scattering length. Furthermore, the scattering length is much smaller than the dimensions of the sample. Therefore the migration of photons is accurately described as a diffusional process. These conditions are met in breast tissue for which the reduced scattering coefficient μ_s' (which is the reciprocal of the photon random-walk step) is approximately 10 cm^{-1} and the absorption coefficient μ_a (which is the reciprocal of the photon absorption length) is approximately 0.03 cm^{-1}.[13,14]

An intensity-modulated source of light produces a wave of light-energy density that propagates spherically outward from the source through the turbid medium. This intensity wave is called a diffuse photon density wave[3,7–9] (DPDW). Although microscopically the photons are diffusing and have thus lost their coherence and memory of their initial direction, macroscopically the photons add incoherently to produce a scalar wave of light-energy density with a well-defined phase front. The wavelength of the DPDW depends on the optical properties and modu-

lation frequency and is ~10 cm for typical biological samples and modulation frequencies (~200 MHz). The optics of DPDW's are understood.[3,7,8,15–20] In particular, studies of the distortion of DPDW's by optical inhomogeneities demonstrate that heterogeneities may be found and characterized by the measurement of distortions in the wave front.[15–18,21,22]

Because measurements are made in the near field (i.e., within one DPDW wavelength of the source), the usual diffraction criteria are inadequate for resolution determinations. In the near field, resolution is intimately related to the signal-to-noise ratio of the measurement. The resolving power of DPDW's has been studied within this context by the comparison of the amplitude of the spatial frequencies with the noise level.[23] Additionally, the resolving power of pulse-time measurements has been examined by the use of temporal point-spread functions.[24–28] No analysis, however, has been made that focuses on limitations for the detection, localization, and characterization of optical inhomogeneities with DPDW's.

In this paper we present such an analysis. We calculate the signals by using a proven analytic model for the scattering of DPDW's from spherical objects.[16–18] Two different noise models are considered: shot noise and random errors that are due to the positional uncertainty of the source and the detector. Our analysis indicates that uncertainties in source, detector, and sample position limits detection to millimeter-sized objects and full optical characterization to centimeter-sized objects. We show how small improvements can be made by optimizing the measurement geometry and source modulation frequency. We find that modulation frequencies of less than 500 MHz are optimal for detection and characterization. For higher modulation frequencies, the noise threshold increases with the modulation frequency more than the relevant signal. In addition, we find that spectral measurements (i.e., by using DPDW information at several modulation frequencies) enhance the characterization of scattering objects but not that of absorbing objects. The clinical relevance of this work is discussed.

2. Models

To determine the limits for detection and characterization of localized heterogeneities, we utilize exact models. A spherical inhomogeneity embedded in an otherwise homogeneous turbid medium is used as the standard system (see Fig. 1) for assessing the limits. The turbid medium is an infinite slab of finite thickness. Measurements are made in the transmission mode at a single-photon wavelength. For an ideal experimental system, the signal-to-noise ratio is shot-noise limited and thus scales with the square root of the number of photons detected. However, there are other sources of random error that exceed shot noise, such as the positional uncertainty of the source and detector relative to the sample. We consider these effects in the subsections below.
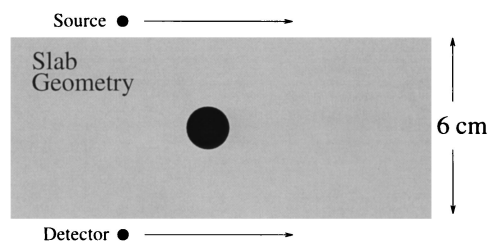
Fig. 1. DPDW's are generated by the injection of light from a sinusoidally modulated source into a turbid medium. The 3-mW, 780-nm source is modulated at 200 MHz. The turbid medium is 6.0 cm thick with a reduced scattering coefficient, μ_s', of 10.0 cm^{-1} and $\mu_a = 0.05$ cm^{-1}. A spherical object is embedded in the middle of the slab. Light is collected and delivered to a photomultiplier tube by means of an optical fiber with a diameter of 0.4 cm. For the simulations, the source and the detector are scanned together along the boundary or the source is held fixed close to the object and the detector is scanned. Two different objects are studied: an absorbing object with $\mu_{s,\,in}' = 10.0$ cm^{-1} and $\mu_{a,\,in} = 0.15$ cm^{-1} and a scattering object with $\mu_{s,\,in}' = 15.0$ cm^{-1} and $\mu_{a,\,in} = 0.05$ cm^{-1}. Other parameters are considered as indicated in the text.

A. Analytic Solution for the Signal

To calculate the signal resulting from the inhomogeneity in Fig. 1, we use the analytic solution for the scattering of the DPDW's from spherical inhomogeneities.[16–18] This method is exact, provided that the diffusion approximation to the transport equation is valid. The analytic solution reveals that the measured DPDW outside the object is simply a superposition of the incident DPDW plus the diffusive wave scattered from the object, i.e.,

$$\Phi(\mathbf{r}_s, \mathbf{r}_d) = S \frac{\exp(ik_{\text{out}}|\mathbf{r}_s - \mathbf{r}_d|)}{4\pi D_{\text{out}}|\mathbf{r}_s - \mathbf{r}_d|} + \sum_{l=0}^{\infty} A_l h_l^{(1)}(k_{\text{out}}r_d)$$
$$\times Y_l^0(\hat{\Omega}_d). \tag{1}$$

Here the position of the source (detector) is denoted by $\mathbf{r}_s$ ($\mathbf{r}_d$) and the object is centered at the origin. S is the modulation amplitude of the source in photons per second. k_{out} is the wave number of the DPDW outside the object and is given by $k_{\text{out}}^2 = (-\nu\mu_{a,\,\text{out}} + i\omega)/D_{\text{out}}$, where ν is the speed of light in the medium, $D_{\text{out}} = \nu/(3\mu_{s,\,\text{out}}')$ is the photon diffusion coefficient, $\mu_{s,\,\text{out}}'$ is the reduced scattering coefficient, $\mu_{a,\,\text{out}}$ is the absorption coefficient of the background medium, and $\omega = 2\pi f$ is the angular frequency of the DPDW (f denotes the modulation frequency). For the scattered wave, $h_l^{(1)}(x)$ are Hankel functions of the first kind and $Y_l^0(\hat{\Omega})$ are the spherical harmonics with the azimuthal index equal to zero, as the source is taken to be on the z axis and the object is at the origin (i.e., the system has azimuthal symmetry). The scattered wave is written as a series of partial waves or multipole moments for which the amplitude of each partial wave is given by the scattering amplitude A_l (see Refs. 16 and 17).

In general, the scattering amplitudes A_l depend on the diameter of the spherical object, the optical properties of the object and the background medium, and the source modulation frequency. Detection and

characterization of the optical inhomogeneities depend on the magnitude of the different partial waves or moments of the scattered DPDW. The most important moments of the scattered wave are the monopole ($\Phi_{sc}^{l=0}$), dipole ($\Phi_{sc}^{l=1}$), and quadrupole ($\Phi_{sc}^{l=2}$). To leading order in $k_{out}a$ and $k_{in}a$, assuming that $|k_{out}a| \ll 1$ and $|k_{in}a| \ll 1$ (where k_{in} is the DPDW wave number inside the spherical object and a is the radius of the object), these moments are

$$\Phi_{sc}^{l=0} = S \frac{\exp(ikr_s)}{4\pi D_{out}r_s} \frac{\exp(ikr_d)}{4\pi r_d} \left(\frac{4\pi a^3}{3}\right)\left(\frac{-\nu\delta\mu_a}{D_{out}}\right), \quad (2)$$

$$\Phi_{sc}^{l=1} = S \frac{\exp(ikr_s)}{4\pi D_{out}r_s} \frac{\exp(ikr_d)}{4\pi r_d} \left(ik - \frac{1}{r_s}\right)\left(ik - \frac{1}{r_d}\right)$$
$$\times (3\cos\theta)\left(\frac{4\pi a^3}{3}\right)\left(\frac{-\delta\mu_s'}{3\mu_{s,out}' + 2\delta\mu_s'}\right), \quad (3)$$

$$\Phi_{sc}^{l=2} = S \frac{\exp(ikr_s)}{4\pi D_{out}r_s} \frac{\exp(ikr_d)}{4\pi r_d} \left(k^2 + \frac{3ik}{r_s} - \frac{3}{r_s^2}\right)$$
$$\times \left(k^2 + \frac{3ik}{r_d} - \frac{3}{r_d^2}\right)(3\cos^2\theta - 1)\left(\frac{4\pi a^5}{45}\right)$$
$$\times \left(\frac{\delta\mu_s'}{5\mu_{s,out}' + 3\delta\mu_s'}\right). \quad (4)$$

Here, $\delta\mu_a = \mu_{a,in} - \mu_{a,out}$ is the difference in the absorption coefficients of the object and the background, $\delta\mu_s' = \mu_{s,in}' - \mu_{s,out}'$ is the difference in the reduced scattering coefficient, $k = k_{out}$, and θ is the angle between the z axis and the line joining the detector to the object center. To leading order $\Phi_{sc}^{l=0}$ depends only on $\delta\mu_a$, and $\Phi_{sc}^{l=1}$ and $\Phi_{sc}^{l=2}$ depend only on $\delta\mu_s'$. We have to look at higher-order terms for the Φ_{sc}^l to see dependences on the other optical properties.

For an object that has the same scattering properties as those of the background, but different absorption properties, the signal is derived to leading order from the monopole term and scales as $a^3\delta\mu_a$. Thus, to leading order, one can only reconstruct the product $a^3\delta\mu_a$ and cannot simultaneously determine the diameter and the absorption coefficient of the object. When the monopole is the only detectable moment, a small, highly absorbing object cannot be distinguished from a larger, less-absorbing object. The dipole and quadrupole moments have a different functional dependence on a and $\delta\mu_a$, and thus the object can be characterized, in principle, when both the monopole and either the dipole or the quadrupole moments are detectable.

The results are similar for an object with a pure scattering change. In that case, the dominant term is the dipole moment, which depends on the product of a^3 and $\delta\mu_s'$. The size and the scattering coefficient of a scattering object, therefore, cannot be simultaneously characterized unless the dipole and the quadrupole moments are detectable. Generally, the detectability of the different moments of the scattered
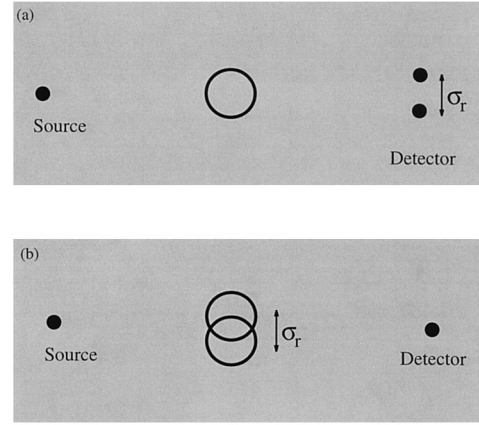

Fig. 2. Errors from positional uncertainty can arise from an inaccurate positioning of the source and the detector relative to each other [as depicted in (a)] or relative to the sample under study [as shown in (b)]. These errors are random unless no vibrations are present and no realignment of the source and the detector are made for multiple measurements. In a clinical environment vibrations will be present that are due to breathing and the heart beat. In case (a) and (b) σ_r is reduced when repeated measurements are made. Positional uncertainties induced by sample vibrations of type (b) are reduced by longer integration times.

DPDW depends on the characteristics of the object and the noise in the measurements.

B. Noise Models

For an ideal experimental system the uncertainty in the measured amplitude and phase of the DPDW is given by shot noise. Shot noise is defined as the square root of the number of photons detected. In practice, however, the uncertainty in the DPDW amplitude and phase is not dominated by shot noise but is also affected by uncertainty in the position of the source and detector relative to one another and relative to the sample (see Fig. 2). There are two different types of positional uncertainty. They are (1) random errors associated with the incorrect positioning of the source and the detector such that the actual distance of the source and detector with respect to each other and with respect to a reference point exhibits a normal distribution about the expected value, and (2) random errors from small motions of the sample, e.g., errors that are due to breathing and the heart pulse. An important difference between these two sources of positional errors is that the second type can be reduced by integration of the signal over longer times whereas the first type, in principle, can reduced only by repeated trials wherein the source and detector are actually repositioned. In our laboratory we have found (in an infinite homogeneous medium) that the positional uncertainty is the leading contributor to the uncertainty in the amplitude and phase of the DPDW. For a given source–detector pair, with a positional uncertainty σ_r, the fractional uncertainty in the amplitude, $\sigma_{AC}/|\Phi(\mathbf{r}_s, \mathbf{r}_d)|$, in an infinite me-

dium is given by

$$\frac{\sigma_{AC}}{|\Phi(\mathbf{r}_s, \mathbf{r}_d)|} = \left[\text{Im}(k) + \frac{1}{|\mathbf{r}_s - \mathbf{r}_d|}\right]\sigma_r$$

$$= \left((3/2)^{1/2}(\mu_a\mu_s')^{1/2}\left\{\left[1 + \left(\frac{\omega}{\nu\mu_a}\right)^2\right]^{1/2} - 1\right\}^{1/2}\right.$$

$$\left. + \frac{1}{|\mathbf{r}_s - \mathbf{r}_d|}\right)\sigma_r, \tag{5}$$

and the uncertainty in the phase in radians, σ_θ, in an infinite medium is given by

$$\sigma_\theta = \text{Re}(k)\sigma_r$$

$$= (3/2)^{1/2}(\mu_a\mu_s')^{1/2}\left\{\left[1 + \left(\frac{\omega}{\nu\mu_a}\right)^2\right]^{1/2} + 1\right\}^{1/2}\sigma_r. \tag{6}$$

$|\Phi(\mathbf{r}_s, \mathbf{r}_d)|$ is the amplitude of the detected DPDW, $\text{Im}(k)$ is the imaginary part of the DPDW wave number, and $\text{Re}(k)$ is the real part of the DPDW wave number. The noise in the amplitude decreases with increasing attenuation length of the DPDW. The noise in the phase decreases with increasing wavelength of the DPDW. Thus a variation of system parameters that results in a decrease in the DPDW attenuation length and wavelength will increase the noise because of source–detector positional uncertainties. We have verified this relation with the equipment in our lab, which has a positional uncertainty of 0.1 mm. To do so, we repeatedly measured the amplitude and phase of the DPDW in an infinite medium at various source–detector separations and compared the measured uncertainties with those we calculated by using Eqs. (5) and (6). This process was then repeated for systems with different optical properties, and in all cases good agreement was observed. Equations (5) and (6) are a reasonable approximation of the amplitude and the phase uncertainties that arise because of positional uncertainties in semi-infinite and slab geometries. For semi-infinite and slab geometries we do not write down the exact equation for the uncertainties. Calculations of the change in amplitude and phase for small displacements of the source and detector for such geometries show that the uncertainties are well approximated by Eqs. (5) and (6).

An estimation of the magnitude of shot noise and noise from positional errors indicates the significance of positional uncertainties. We estimate a clinically relevant shot noise by using a 3-mW light source with 100% modulation, a detector with a collection area of 0.1 cm^2, a quantum efficiency of 1%, and the experimental system depicted in Fig. 1. With these parameters, shot noise gives a fractional error of 9×10^{-4} in the wave amplitude for a 1-s integration time (the phase noise is 9×10^{-4} rad or $\sim 0.05°$). For a positional uncertainty of 10 μm in either the source or the detector, the fractional error in the amplitude is 2×10^{-3} and the phase noise is 0.03°. If the uncertainty is in the position of both the source and the detector then the noise threshold is multiplied by

$\sqrt{2}$. For a typical clinical situation the noise produced from positional uncertainties in the source and detector is comparable with shot noise.

Achieving a positional certainty of 10 μm in the clinic is a daunting task, considering the motional artifacts arising from the respiration and pulse of the subjects. A more realistic positional uncertainty of 100 μm will result in a 2% uncertainty in the amplitude and a 0.3° uncertainty in the phase. These results are for a best case and are based on the shot noise's arising under the above-described conditions and the additional noise's arising from a positional uncertainty of 10 μm. These two types of noise are reduced by the $\sqrt{N}$, where N is the number of independent measurements averaged to obtain a single value for the amplitude and the phase.

3. Description of Simulations

All results in this section for the detection and characterization of optical inhomogeneities by DPDW's are based on analytic calculations of the distorted DPDW with appropriate levels of random noise. The sample is an infinite slab, 6 cm thick (~ 60 random-walk steps thick), which is homogeneous except for a spherical heterogeneity centered between the input and the output planes of the slab. Measurements are made in the transmission mode, i.e., the source is on one side of the slab and the detector is on the other side. Two types of spherical objects are considered: an absorbing object that has the same scattering coefficient as that of the background and a scattering object that has the same absorption coefficient as that of the background.

For studying the limits for detection and localization of these objects, the source and detector are scanned together along the surface of the slab. The perturbation to the amplitude and the phase of the DPDW by the object can be described, respectively, by the ratio of the amplitudes with and without the object and the difference in the phase with and without the object.

In Section 4 the detectability of the object is found by a comparison of this perturbation with the noise level. If the perturbation is greater than the noise level, the object is deemed detectable. We study a large portion of parameter space by varying the background optical properties, the object optical properties, and the DPDW modulation frequency. Note that at each detector position the signal is integrated for 1 s and measured once. Shot noise can be reduced by an increase in the integration time, and the noise that is due to positional errors can be reduced by the averaging of repeated measurements in which the source and the detector are physically repositioned. If the positional errors are due to movement of the sample, then the noise is also reduced by an increase in the integration time.

The ultimate clinical applications of these probes may depend on our capabilities for object characterization. For example, to specify tumor size and malignancy or brain bleed maturity, it is likely that the size and optical properties of the detectable optical

inhomogeneity will need to be characterized. In Section 5 limits to object characterization are studied first by the calculation of the perturbed DPDW and then by the estimation of the uncertainty with which the object's size and optical properties can be determined by means of a chi-squared fitting procedure to the analytic solution. The perturbed DPDW is first calculated by the use of the analytic solution, and then appropriate noise is added. Simulated measurements are made with the source fixed at a position closest to the object at $x = 0$ and $z = 0$, and the detector is scanned from $x = -2.0$ to 2.0 cm in steps of 0.20 cm at $z = 6.0$ cm. A total of 42 independent measurements are obtained (21 amplitude and 21 phase measurements). In all studies the DPDW modulation frequency is 200 MHz. The noise added in these measurements is that given by the shot noise for a 3-mW source and the noise from random positional uncertainties of 10 μm, as described in subsection 2B. Thus the noise used in the simulations is approximately 0.3% in the amplitude and 0.08° in the phase.

The fitting procedure is based on minimizing the chi-squared difference between the measured DPDW profile and the analytic solution by varying the object's diameter and optical properties. This procedure is a best case, as we assume the background optical properties as well as the position and shape of the object. In practice, more general imaging methods must be used that do not assume that the shape of the object is known. Our results therefore represent the best one can possibly do in terms of characterization for a specific set of measurements. For a given noise level, the uncertainty in the estimated properties is found with the chi-squared method described by Bevington.[29] In essence, the uncertainty of a fit parameter is found when the parameter is varied until the chi-squared value increases by one from the value at the global minimum. Theoretically, the uncertainty determined in this way is equivalent to the uncertainty that would be found from multiple experiments.

The chi-squared difference function to be minimized is

and a). Recall that $\Phi^i_{\exp}(\mathbf{r}_s{}^i, \mathbf{r}_d{}^i)$ is obtained by the addition of random noise to the analytic solution [Eq. (1)]. The vertical bars, $|\Phi|$, indicate the absolute value of the complex number, and $\arg[\Phi]$ represents the phase of the complex number Φ.

The initial amplitude and phase of the source are known. Uncertainty in the amplitude and phase of the source introduces systematic errors, further complicating the characterization procedure. If such uncertainty is present, then the initial phase and amplitude of the source can also be used as free parameters in the chi-squared fit at the expense of increasing the uncertainty in the other fitting parameters.

4. Detection and Localization

Breast tumors and brain bleeds are optical inhomogeneities in the sense that their optical scattering and absorption properties are different from those of the surrounding media. An understanding of the detection limits of these inhomogeneities is important for designing optical screening techniques. An optical inhomogeneity is said to be detectable if the perturbation to the detected amplitude or phase of the DPDW is larger than the noise threshold.

We can detect absorbing objects as small as 3 mm when the object absorption coefficient is a factor of 3 larger than the background. We can detect scattering objects as small as 4 mm when the object scattering coefficient is a factor of 1.5 larger than the background. The small absorbing objects are detectable because of perturbations to the amplitude of the DPDW, whereas scattering objects are detectable because of perturbations to the phase of the DPDW. The detectability of objects with different contrast is determined by the $a^3\delta\mu_a$ ($a^3\delta\mu'_s$) dependence of the leading-order multipole moment of the DPDW scattered from an absorbing (scattering) object. Generally the detectability of an object is determined by the magnitude of $a^3\delta\mu_a$ or $a^3\delta\mu'_s$. For example, if a 3-mm-diameter absorber with $\delta\mu_a = 0.10$ cm^{-1} is detectable, then a 1-mm object with $\delta\mu_a = 2.7$ cm^{-1} is also detectable for the same sys-

$$\chi^2(\mu'_s, \mu_a, a) = \sum_{i=1}^{N} \frac{\left[|\Phi^i_{\exp}(\mathbf{r}_s{}^i, \mathbf{r}_d{}^i)| - |\Phi^i_{\text{anal}}(\mathbf{r}_s{}^i, \mathbf{r}_d{}^i, \mu'_{s,\text{in}}, \mu_{a,\text{in}}, a)|\right]^2}{\sigma^{i2}_{\text{AC}}}$$
$$+ \frac{\{\arg[\Phi^i_{\exp}(\mathbf{r}_s{}^i, \mathbf{r}_d{}^i)] - \arg[\Phi^i_{\text{anal}}(\mathbf{r}_s{}^i, \mathbf{r}_d{}^i, \mu'_{s,\text{in}}, \mu_{a,\text{in}}, a)]\}^2}{\sigma^{i2}_{\theta}}. \quad (7)$$

Here, the sum is over all measurements, $\mathbf{r}_s{}^i$ and $\mathbf{r}_d{}^i$ are the position of the source and the detector for the ith measurement, respectively, $\Phi^i_{\exp}(\mathbf{r}_s{}^i, \mathbf{r}_d{}^i)$ is the experimental photon fluence for this pair, and $\Phi^i_{\text{anal}}(\mathbf{r}_s{}^i, \mathbf{r}_d{}^i, \mu'_{s,\text{in}}, \mu_{a,\text{in}}, a)$ is the fluence obtained from the analytic solution [Eq. (1)] by the use of the optical characteristics of the object (i.e., $\mu'_{s,\text{in}}$, $\mu_{a,\text{in}}$,

tem. This rule of thumb is discussed further in Section 7.

A. Detection of Absorbing Objects

Figure 3 plots the change in the amplitude and phase of the DPDW that is due to a spherical absorber with $\mu_{a,\text{in}} = 0.15$ cm^{-1} embedded in a system with $\mu'_{s,\text{out}}$
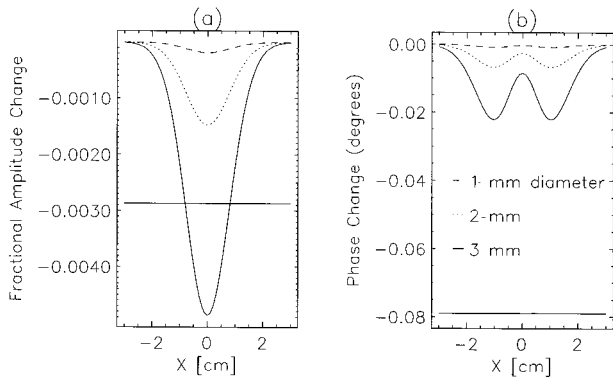
Detection of Absorbing Objects

Fig. 3. (a) Fractional change in the amplitude. (b) Change in degrees of the phase that are due to the presence of the absorbing object as functions of the lateral position of the source–detector. The system is described in the caption of Fig. 1. Results are given for 1.0-mm- (dashed curve), 2.0-mm- (dotted curve), and 3.0-mm- (solid curve) diameter absorbers. The noise threshold is given by the solid horizontal line. Note that the signal does not exceed the noise threshold unless the object's diameter is greater than or equal to 3.0 mm, and then it is only the change in the amplitude and not the phase that is detectable.

$= 10.0$ cm^{-1} and $\mu_{a, \text{out}} = 0.05$ cm^{-1}. Details of the system are described in Fig. 1. Results are plotted for 1-mm-, 2-mm-, and 3-mm-diameter absorbers. Given the above-discussed noise threshold, the absorber can be detected if its diameter is at least 3 mm. Note that the largest change in the signal occurs when the object lies directly between the source and detector. Thus if the object is detectable, its transverse position can be determined. When the source and detector are scanned along three orthogonal axes, the central coordinates of a detectable object are easily determined. The certainty in the determined position of the object is in principle set by the accuracy in the position of the source and detector.

Figure 4 presents contour plots of the smallest detectable absorber for a large portion of parameter space. Note that the noise levels depend on the factors that are being varied in these graphs and are therefore not fixed at the levels used in Fig. 3. For example, with a 200-MHz modulation frequency with $\mu_s' = 20.0$ cm^{-1} and $\mu_a = 0.05$ cm^{-1}, the fractional error in the amplitude is 0.7% and the phase error is 0.3°. With a 200-MHz modulation frequency with $\mu_s' = 10.0$ cm^{-1} and $\mu_a = 0.15$ cm^{-1}, the fractional error in the amplitude is 1% and the phase error is 0.4°. Recall that with a 200-MHz modulation frequency with $\mu_s' = 10.0$ cm^{-1} and $\mu_a = 0.05$ cm^{-1}, the fractional error in the amplitude is 0.3% and the phase error is 0.08°, so that in Fig. 4 the noise levels are varying by at least a factor of 5. The noise levels are still determined with a 1-s integration time.

In Fig. 4(a), the contours indicating the diameter of the smallest detectable absorber are drawn as a function of the background reduced scattering coefficient and the object absorption coefficient. The background absorption coefficient was kept fixed and the object reduced scattering coefficient was kept equal to
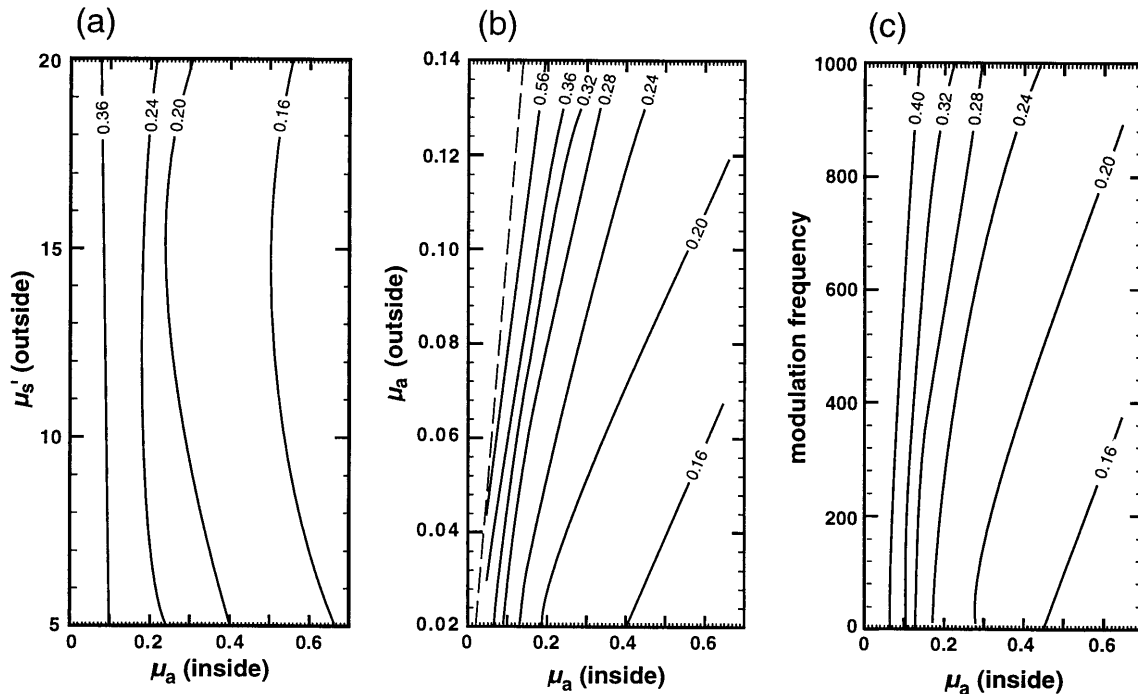
Fig. 4. Diameter of the smallest detectable absorber is plotted as a function of (a) $\mu_{s, \text{out}}'$ and $\mu_{a, \text{in}}$, (b) $\mu_{a, \text{out}}$ and $\mu_{a, \text{in}}$, (c) source modulation frequency and $\mu_{a, \text{in}}$. The contours indicate the diameter of the smallest detectable absorber in units of centimeters. The system and measurements are described in Fig. 1. In (a), $f = 200$ MHz, $\mu_{a, \text{out}} = 0.05$ cm^{-1}, and $\mu_{s, \text{in}}' = \mu_{s, \text{out}}'$. In (b), $f = 200$ MHz and $\mu_{s, \text{out}}' = \mu_{s, \text{in}}' = 10.0$ cm^{-1}. In (c), $\mu_{s, \text{out}}' = \mu_{s, \text{in}}' = 10.0$ cm^{-1}, and $\mu_{a, \text{out}} = 0.05$ cm^{-1}. The noise levels are based on a positional uncertainty of 10 µm and a 1-s integration time.

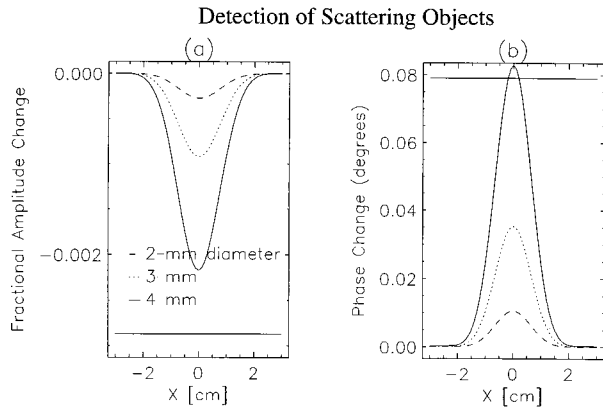Detection of Scattering Objects

Fig. 5.   (a) Fractional change in the amplitude.   (b) Change in degrees of the phase that are due to the scattering object as functions of the lateral position of the source–detector.   The solid curves correspond to a 0.4-cm-diameter object, and the dotted and the dashed curves correspond to a 0.3-cm- and 0.2-cm-diameter object, respectively.   System parameters are described in the caption of Fig. 1.   The noise threshold is given by the solid horizontal line and is 0.3% for the amplitude change and 0.08° phase.   The scattering object is detectable when the diameter is 0.40 cm because the phase change exceeds the noise threshold.

the background reduced scattering coefficient. Clearly, as the object absorption coefficient increases, smaller objects become detectable.   The background reduced scattering coefficient has little effect on absorber detectability, which indicates that the increasing noise, resulting from a larger $\mu'_{s,\,out}$, is balanced by an increasing signal.   The noise increases because of reduced photon transmission through the slab with increased μ'_s.   In Fig. 4(b), contours are drawn as functions of the background and the object absorption coefficients while the scattering coefficients are kept constant.   The detectability of absorbers diminishes as the background absorption coefficient rises because of an increase in shot noise (which is due to increased photon absorption) and the decrease in the absorption contrast of the object.   In Fig. 4(c), contours are given as a function of source modulation frequency and object absorption coefficient.   Surprisingly, increasing the modulation frequency actually decreases the detectability of absorbers.   This trend is observed because the noise increases more rapidly than the signal, as discussed further in Subsection 7.B and Fig. 12.

B.   Detection of Scattering Objects

Figure 5 graphs the relative change in the signal that is due to an object with a reduced scattering coefficient that is different from that of the background. From Fig. 5 we see that a 0.4-cm-diameter object with a 50% increase in μ'_s relative to the background is detectable.   A small scattering object is detectable because the phase shift exceeds the noise threshold, whereas a small absorbing object is detectable because of the relative change in the amplitude.   It is because of this distinction that one can ultimately distinguish absorbing and scattering objects.   Local-

ization of a scattering object is straightforward, as the largest change in the phase occurs when the object is directly between the source and the detector.

Contour plots of the smallest detectable scattering object are presented in Fig. 6.   In Fig. 6(a), the smallest detectable object is plotted as a function of background and object reduced scattering coefficients. These results corroborate our expectations that smaller scatterers can be detected when the scattering contrast is increased.   In Fig. 6(b), results are plotted as a function of background absorption coefficient and object scattering coefficient.   The object absorption coefficient is kept the same as that of the background.   The background absorption coefficient has little effect on the detectability of scattering objects except when the scattering contrast is large.   In Fig. 6(c), results are plotted as a function of source modulation frequency and object scattering coefficient.   The detectability of the scattering object is relatively unaffected by an increase in the modulation frequency, indicating that the noise and the signal are increasing at the same rate.   In contrast, for the absorbing object, the detectability decreased because the noise increased more than the signal.

5.   Characterization

After a tumor or brain bleed has been detected and localized, we can then derive information about the inhomogeneity's physical and physiological state by characterizing its size and optical properties.   As seen in Figs. 3 and 5, the amplitude and phase profile of a distorted DPDW are sensitive to the size of the inhomogeneity as well as to the optical properties. Thus, in principle, the characteristics of an inhomogeneity can be determined from the profile of the distorted DPDW.   However, in contrast to localization, the size and optical properties cannot be determined directly.   We must rely on indirect methods, such as image reconstruction techniques or best fits to analytic solutions for the measured DPDW profile, in order to deduce this information.   As described in the experimental section (Section 3), we use chi-squared fitting techniques to fit for the size and optical properties of the optical inhomogeneity.

A.   Characterization of Absorbing Objects

First we consider simultaneous characterization of the diameter and the absorption coefficient of an absorbing object embedded in the center of a 6-cm-thick slab (see Fig. 1).   The scattering coefficient of the object is the same as that of the background, and the detector is scanned from $x = -2.0$ to 2.0 cm in steps of 0.2 cm, whereas the source is fixed nearest the object at $x = 0$.   Figure 7 presents contour plots of the fractional uncertainties of the object's diameter and absorption coefficient.   Three different contour plots are given: in Figs. 7(a) and 7(b), results are given versus object diameter and absorption coefficient ($\mu'_{s,\,out} = \mu'_{s,\,in} = 10.0$ cm^{-1}, $\mu_{a,\,out} = 0.05$ cm^{-1}, and $f = 200$ MHz).   In Figs. 7(c) and 7(d), results are given versus background reduced scattering coefficient and object absorption coefficient ($\mu'_{s,\,in} = \mu'_{s,\,out}$,

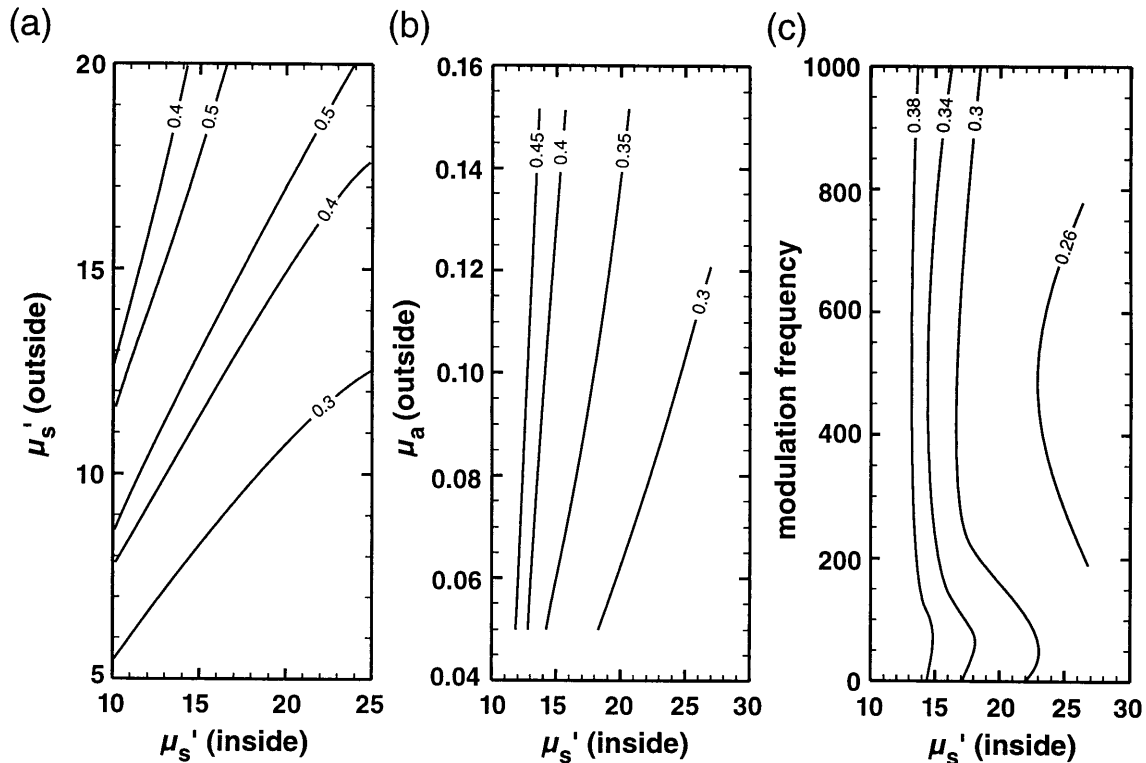Fig. 6. Diameter of the smallest detectable scatterer plotted as a function of (a) $\mu'_{s,\,out}$ and $\mu'_{s,\,in}$, (b) $\mu_{a,\,out}$ and $\mu_{s,\,in}$, (c) source modulation frequency and $\mu_{s,\,in}$. The contours indicate the diameter of the smallest detectable scatterer in units of centimeters. The system and measurements are described in Fig. 1. In (a), $f = 200$ MHz and $\mu_{a,\,out} = \mu_{a,\,in} = 0.05$ cm^{-1}. In (b), $f = 200$ MHz, $\mu'_{s,\,out} = 10.0$ cm^{-1}, and $\mu_{a,\,out} = \mu_{a,\,in}$. In (c), $\mu'_{s,\,in} = 10.0$ cm^{-1} and $\mu_{a,\,out} = \mu_{a,\,in} = 0.05$ cm^{-1}. The noise levels are based on a positional uncertainty of 10 μm and a 1-s integration time.

$\mu_{a,\,out} = 0.05$ cm^{-1}, diameter = 1.2 cm, and $f = 200$ MHz). In Figs. 7(e) and 7(f), results are given versus background absorption coefficient and object absorption coefficient ($\mu'_{s,\,out} = \mu'_{s,\,in} = 10.0$ cm^{-1}, diameter = 1.2 cm, and $f = 200$ MHz). The system is described in more detail in Fig. 1. These three contour plots reveal the variation in fractional uncertainty over a large sampling of the parameter space. The magnitude of the uncertainty depends on the total number of measurements that are considered in the chi-squared fit and in general decreases as the square root of the number of measurements. For the parameter space considered in Fig. 7, we see that, given 21 measurements of the phase and the amplitude (for a total of 42 independent measurements), the absorbing object can be accurately characterized when its diameter exceeds 0.8 cm. Here an uncertainty of 20% or less is considered to be accurate.

The contour plots versus the object's diameter and absorption coefficients [Figs. 7(a) and 7(b)] show that the uncertainties diminish rapidly as the diameter increases and slowly as the absorption coefficient is increased. The slower decrease in the uncertainties for larger absorption coefficients results from saturation of the signal. In general the error bar for the diameter is symmetric about the mean value whereas the error bar for the absorption coefficient of the object is asymmetric. The asymmetry results from the saturation of the signal for larger absorption coeffi-

cients. Thus the upper error is always larger than the lower error. The difference is usually within 20%. In all contour plots we plot the average of the lower and upper fractional uncertainties.

From the contour plots versus the background reduced scattering coefficient and the object absorption coefficient [Figs. 7(c) and 7(d)] we see a similar dependence on the absorption coefficient of the object and that the uncertainties initially decrease and then increase as $\mu'_{s,\,out}$ increases. The explanation for this is that as $\mu'_{s,\,out}$ increases, the DPDW wavelength decreases, and as the ratio between the DPDW wavelength and the object diameter becomes smaller, the fractional perturbation to the signal increases. Therefore we would expect the uncertainties in the fitting parameters to decrease. However, the noise from positional errors is also increasing because the DPDW wavelength is decreasing. In addition, the shot noise is increasing because of the reduced transmission through the slab as μ'_s is increased. For the conditions in Figs. 7(c) and 7(d) the interplay between the increasing signal and the increasing noise is such that the uncertainties first decrease and then increase.

From the contour plots versus the background absorption coefficient and the object absorption coefficient [Figs. 7(e) and 7(f)], we see that the uncertainties increase as the background absorption coefficient is increased, and they decrease as the ob-

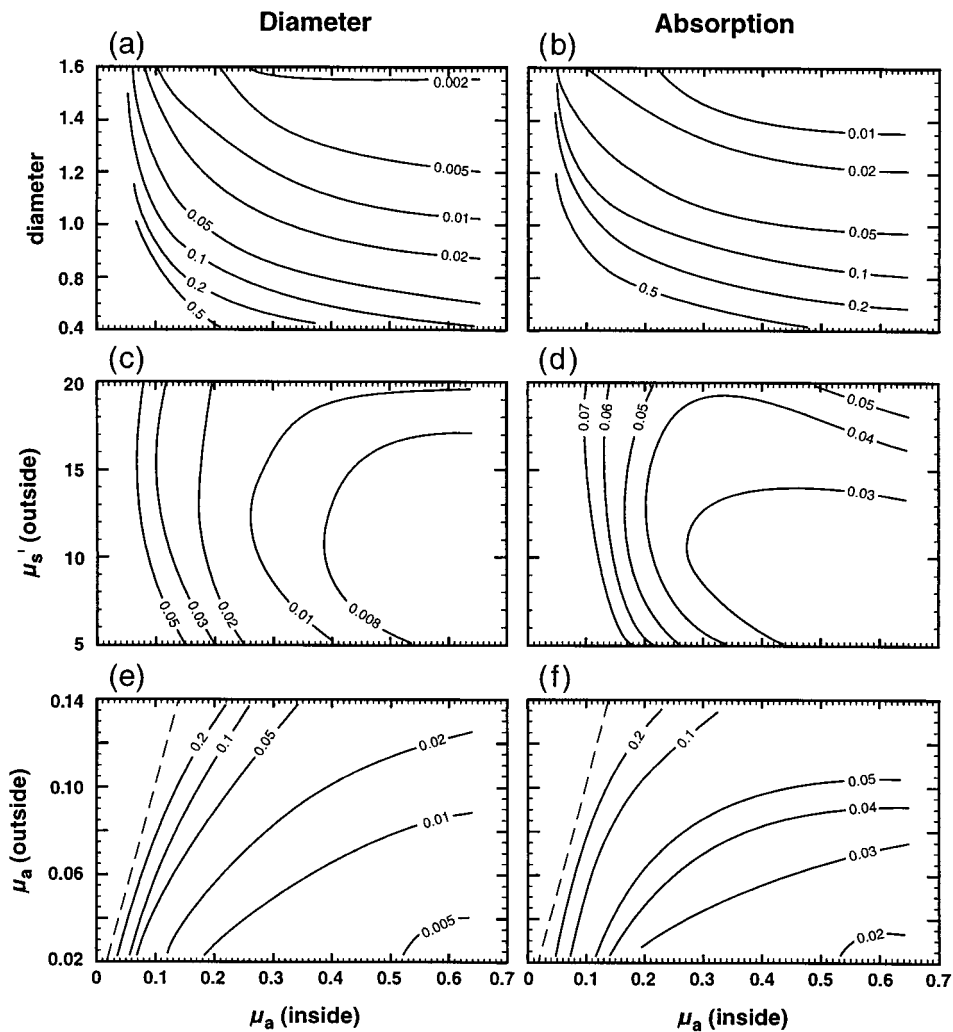**Fractional Error in**

| Diameter | Absorption |

Fig. 7. Fractional uncertainties in (a), (c), (e) the object diameter, (b), (d), (f) the object absorption coefficient plotted in contour plots for a large range of parameter space. The labels on the contours indicate the fractional uncertainty. In (a) and (b) uncertainties are plotted versus the diameter and absorption coefficient of the object. In (c) and (d) the background scattering coefficient and object absorption coefficient are varied. In (e) and (f) the background absorption coefficient and object absorption coefficient are varied. The dashed curves in (e) and (f) indicate where μ_a(outside) = μ_a(inside).

ject absorption coefficient is increased. There are two factors contributing to the dependence on the background absorption coefficient: first, more light absorption leads to an increase in shot noise, and second, the decrease in the absorption contrast of the object results in a smaller perturbation to the DPDW.

Although a 0.3-cm-diameter absorber can be detected and localized, the absorber cannot be characterized accurately unless its diameter is greater than ~0.8 cm. This result was obtained from 21 measurements of amplitude and phase. As discussed in Subsection 2.A, this difference between object detection and characterization arises from the functional form of the different moments of the scattered DPDW. Figure 8 plots the contribution of the monopole, dipole, and quadrupole moments of the scattered DPDW to the total signal versus the diameter of the absorbing object. That is, we plot the amplitude and

phase of

$$\Phi_{\mathrm{sc}}^{(l)}/\Phi_{\mathrm{inc}}. \qquad (8)$$

Note that this ratio accounts for the perturbation of each moment to the incident DPDW. If this ratio is greater than the noise threshold, the given moment of the scattered wave is detectable. The noise threshold is also indicated in Fig. 8.

In order to detect the object it is necessary for only the monopole term to exceed the noise threshold. As seen in Fig. 8, this occurs when the object's diameter is ≥0.3 cm, which agrees with the previous observation in Fig. 3. The dipole moment does not exceed the noise threshold until the diameter is ≥0.8 cm. For absorber diameters ≥0.8 cm the monopole and the dipole moments of the scattered wave are detect-
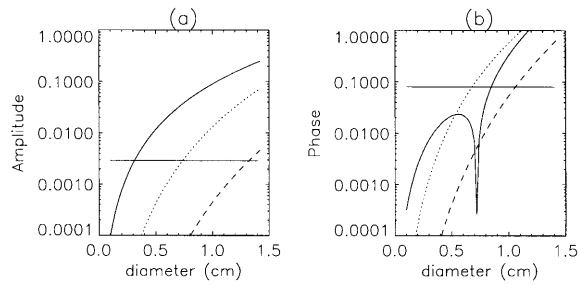
Fig. 8. (a) Amplitude, (b) phase contributions of the monopole (solid curves), dipole (dotted curves), and quadrupole (dashed curves) moments of the scattered wave to the incident wave graphed versus the diameter of the absorbing object. The noise threshold is indicated by the horizontal line at 2.9×10^{-3} for the amplitude and 8×10^{-2} for the phase. When the monopole term exceeds the noise threshold at 0.3 cm, the absorber is detectable. However, the diameter and the absorption coefficient of the absorber cannot be simultaneously determined until the monopole and dipole terms are detectable. This is the case for diameters greater than 0.8 cm.

able and thus, in principle, the absorber is characterizable. The results in Fig. 7 indicate that the absorber can be accurately characterized when the diameter exceeds 0.8 cm. Recall that the uncertainty in the object parameters decreases with the square root of the number of measurements, and thus accurate characterization of smaller objects is possible by an increase in the number of measurements. This may give an experimenter an improvement of 0.3 cm if, for example, 400 measurements are made of the scattered DPDW over the same spatial region as the 40 measurements. This 0.3-cm improvement is estimated from Fig. 8; if the number of measurements is increased by a factor of 10 then the uncertainty will decrease by approximately a factor of 3. Thus, from Fig. 8, we see that the monopole and the dipole contributions exceed the noise threshold when the diameter of the absorber exceeds 0.5 cm.

B. Characterization of Scattering Objects

Here we consider the simultaneous characterization of the diameter and the scattering coefficient of a scattering object embedded in the center of a 6-cm-thick slab (see Fig. 1). The absorption coefficient of the object is the same as that of the background, and the detector is scanned from $x = -2.0$ to 2.0 cm in steps of 0.2 cm whereas the source is fixed nearest the object at $x = 0$. Figure 9 presents contour plots of the fractional uncertainty of the object's diameter and scattering coefficient. Three different contour plots are given: in Figs. 9(a) and 9(b), results are given versus object diameter and scattering coefficient ($\mu'_{s, \text{out}} = 10.0 \text{ cm}^{-1}$, $\mu_{a, \text{out}} = \mu_{a, \text{in}} = 0.05 \text{ cm}^{-1}$, and $f = 200$ MHz). In Figs. 9(c) and 9(d), results are given versus background reduced scattering coefficient and object reduced scattering coefficient ($\mu_{a, \text{out}} = \mu_{a, \text{in}} = 0.05 \text{ cm}^{-1}$, diameter = 1.2 cm, and $f = 200$ MHz). In Figs. 9(e) and 9(f) results are given versus background absorption coefficient and object reduced scattering coefficient ($\mu'_{s, \text{out}} = 10.0 \text{ cm}^{-1}$, $\mu_{a, \text{out}} =$

$\mu_{a, \text{in}}$, diameter = 1.2 cm, and $f = 200$ MHz). The system is described in more detail in Fig. 1. By plotting these three contour plots, we see the variation in the fractional uncertainty over a large sampling of the parameter space. The magnitude of the uncertainty depends on the total number of measurements that are considered in the chi-squared fit and, in general, decreases as the square root of the number of measurements. For the parameter space considered in Fig. 9, we see that, given 21 measurements of the phase and amplitude (for a total of 42 independent measurements), the scattering object can be accurately characterized when its diameter exceeds 0.8 cm. The exact value depends on the scattering coefficient of the object. Again an uncertainty of less than 20% is considered accurate.

From the contour plots versus the object's diameter and scattering coefficient [Figs. 9(a) and 9(b)], we see that the uncertainties diminish rapidly as the diameter increases and slowly as the reduced scattering coefficient is increased. The slower decrease in the uncertainties for larger scattering coefficients results from saturation of the signal and the leading order $a^3 \delta \mu'_s$ dependence of the scattered wave. Note that, in general, the error bar for the diameter is symmetric about the mean value whereas the error bar for the scattering coefficient of the object is asymmetric. The asymmetry results from the saturation of the signal for larger scattering coefficients, and thus the upper error is always larger than the lower error. The difference is usually within 20%. In all contour plots we plot the average of the lower and the upper fractional uncertainties.

From the contour plots versus the background reduced scattering coefficient and the object reduced scattering coefficient [Figs. 9(c) and 9(d)] we first see that the object cannot be characterized when the scattering contrast is smaller than 40%. Interestingly, the fractional uncertainty changes more with a change in the background scattering coefficient than with a change in the object scattering coefficient. One might expect that the uncertainty depends on only the difference in the scattering coefficients, in which case changes in the fractional uncertainty would be symmetric with respect to changes in the scattering coefficient of the background and the object. The observed asymmetry results from the noise's dependence on the background reduced scattering coefficient. As the background reduced scattering coefficient is increased, the noise also increases because of the reduced transmission of light through the slab (shot noise) and the decrease in the DPDW wavelength.

From the contour plots versus the background reduced scattering coefficient and the object absorption coefficient [Figs. 9(e) and 9(f)], we see that the uncertainties increase slightly with an increase in the absorption coefficient and decrease with an increase in the object reduced scattering coefficient. These trends are simply due to the increased shot noise from increasing the background absorption coeffi-
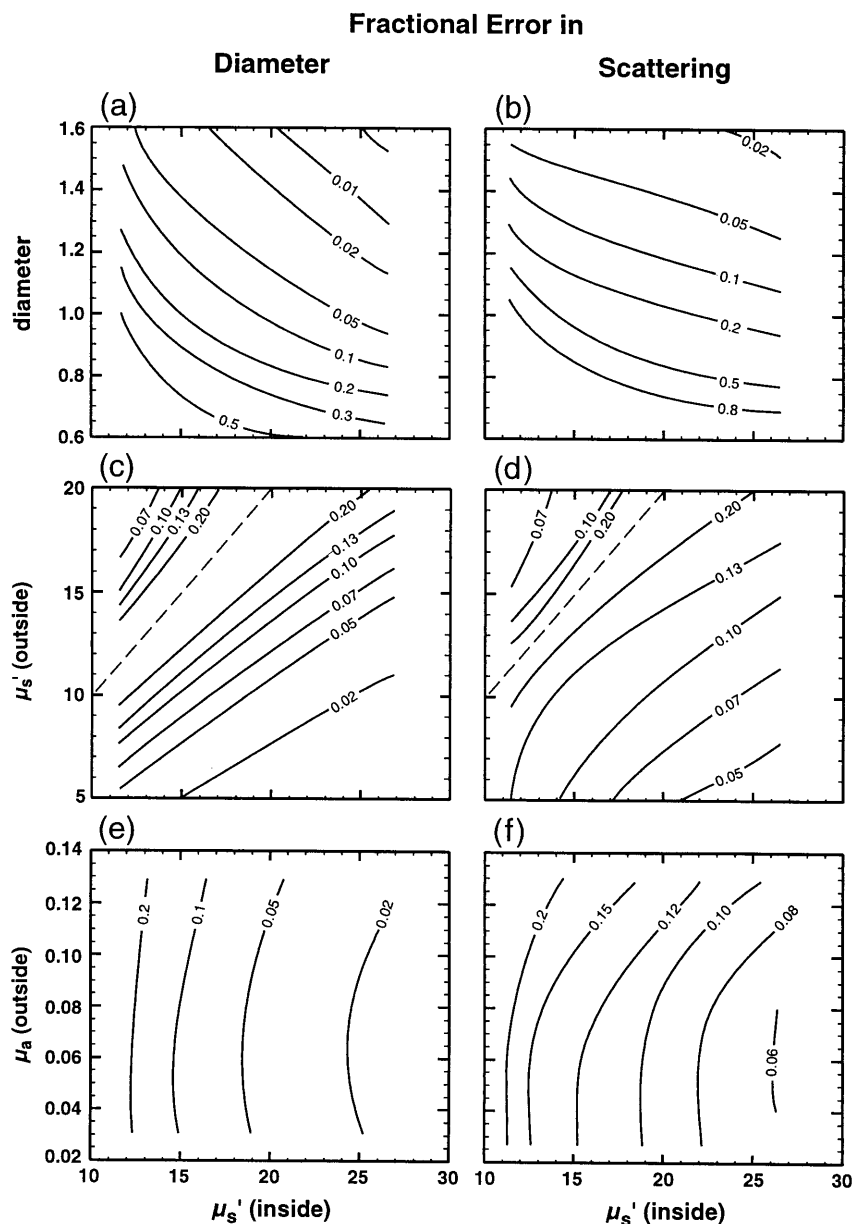
Fractional Error in

Fig. 9.   Fractional uncertainties in (a), (c), (e) the object diameter, (b), (d), (f) the object scattering coefficient plotted in contour plots.   The labels on the contours indicate the fractional uncertainty.   In (a) and (b) uncertainties are plotted versus the diameter and the scattering coefficient of the object.   In (c) and (d) the background scattering coefficient and the object scattering coefficient are varied.   In (e) and (f) the background absorption coefficient and the object scattering coefficient are varied.   The dashed curves in (c) and (d) indicate where μ_s'(outside) = μ_s'(inside).

cient and the increased signal from increasing the object reduced scattering coefficient.

Although a 0.4-cm-diameter scatterer can be detected and localized, the scatterer cannot be characterized accurately unless its diameter is greater than 0.8 cm.   As discussed above, this difference between object detection and characterization arises from the functional form of the different moments of the scattered DPDW.

6.   Optimizing the Experimental Design

Improvements in detecting and characterizing optical inhomogeneities are generally achieved by an in-

crease in the signal relative to the noise.   We can reduce the noise threshold by making multiple measurements or by integrating the signal longer and reducing shot noise and positional error that are due to sample motions.   These noise-reduction techniques reduce the noise by the square root of the number of measurements or the square root of time. The magnitude of the perturbation can be increased by an increase in the modulation frequency.   Increasing the modulation frequency decreases the DPDW wavelength, which in turn results in a larger scattering amplitude, particularly for the higher moments.   However, increasing the modulation fre-
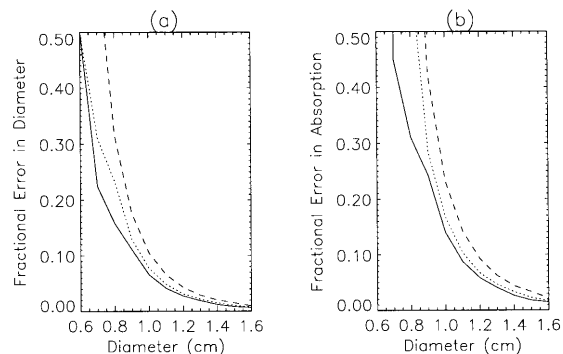
Fig. 10. Fractional uncertainties for (a) the object diameter, (b) the object absorption coefficient are plotted versus the known object diameter for different sets of measurements. The solid curves correspond to the set of measurements presented in Fig. 7, that is, the detector is scanned from $x = -2.0$ to 2.0 cm whereas the source is fixed at $x = 0$. The dotted curves correspond to keeping the source fixed at $x = 0$ and scanning the detector from $x = -3.0$ to 3.0 cm, whereas for the dashed curves the source and the detector were scanned together from $x = -3.0$ to 3.0 cm. In all cases 21 independent measurements of the phase and the amplitude were obtained at even intervals over the range of the scan. The system parameters are described in Fig. 1.

quency will increase the shot noise, as a result of the reduced DPDW amplitude for the same source–detector separation, and increase the uncertainty that is due to positional errors, as a result of the reduced DPDW wavelength. In the subsections below we investigate the interplay between these various factors.

A. Optimizing Measurement Geometry

To determine what role the positions of the source and the detector play in characterizing an object, we repeated the characterization simulation for two different measurement geometries. First the effect of fixing the source closest to the object at $x = 0$ and scanning the detector from $x = -3.0$ to 3.0 cm in steps of 0.30 cm was examined. The fractional uncertainties in the diameter and absorption coefficient for this set of measurements are graphed in Fig. 10 along with the previous results obtained when the detector was scanned from $x = -2.0$ to 2.0 cm in steps of 0.20 cm. These results indicate that the characterization accuracy is decreased when the range over which the detector is scanned is increased while the number of measurements is kept constant. The second measurement geometry was chosen to examine the effect of scanning the source and the detector together from $x = -3.0$ to 3.0 cm. For comparison, these results are also plotted in Fig. 10. The characterization accuracy is decreased further when the source and detector are scanned together. From Fig. 10 we see that the measurement geometry is optimized for object characterization by keeping the source and detector near the absorbing object. This result applies to scattering objects as well.

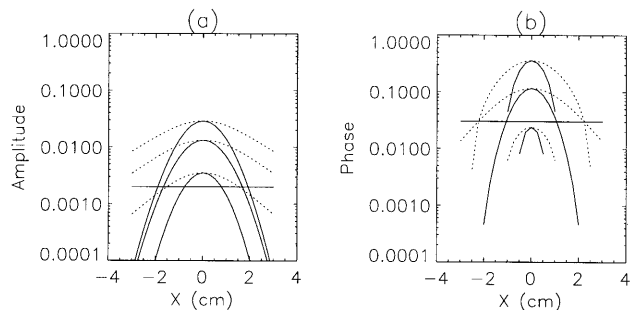These observations are easily understood within the context of the moments analysis. Figure 11

Fig. 11. (a) Amplitude, (b) phase contributions of the monopole, dipole, and quadrupole moments of the scattered wave to the incident wave are graphed versus the lateral position of the detector. The source was scanned with the detectors for the solid curves and fixed at $x = 0$ for the dashed curves. At $x = 0$ the top, middle, and bottom pairs of solid and dashed curves correspond respectively to the contributions of the monopole, dipole, and quadrupole moments. The noise threshold is indicated by the horizontal line at 2×10^{-3} for the amplitude and 3×10^{-2} for the phase. When the source is fixed at $x = 0$, i.e., near the object, the signal is larger, permitting an accurate characterization of smaller objects.

graphs the contribution of each moment to the total signal [Eq. (8)] versus the transverse position of the detector. Results are plotted for two cases: (1) the source is scanned with the detector, and (2) the source is fixed at $x = 0$. The moments are calculated for a 1.0-cm-diameter absorber. From Fig. 11 we see that, overall, the moments make a larger contribution to the scattered wave when the source is fixed near the object. In particular, the perturbation is larger for transverse displacements of the detector from $x = 0$, and therefore it is detectable for a greater number of measurements. By concentrating the measurements where the perturbation is strongest, we are increasing the average signal-to-noise ratio, resulting in a more accurate determination of an object's characteristics.

This result suggests that the most accurate characterization will arise from all measurements coming from the source and the detector fixed nearest the object. This is indeed the case when there are only two unknowns, e.g., diameter and absorption coefficient. That is, the amplitude and the phase from one source–detector pair provide sufficient information to determine two unknowns. However, if there are more than two unknowns (e.g., initial amplitude and phase of the source, object shape, or object position in addition to the diameter and absorption coefficient of the object), then the additional information provided from a spatially distributed set of source–detector pairs is required.

Usually the initial amplitude and phase of the source and the shape of the object will not be known accurately, and therefore measurements from a spatially distributed set of source–detector pairs is optimal. The signal-to-noise comparison in Fig. 11 indicates which measurements provide information about the optical inhomogeneity and therefore provide an approach for designing an optimal measurement geometry.
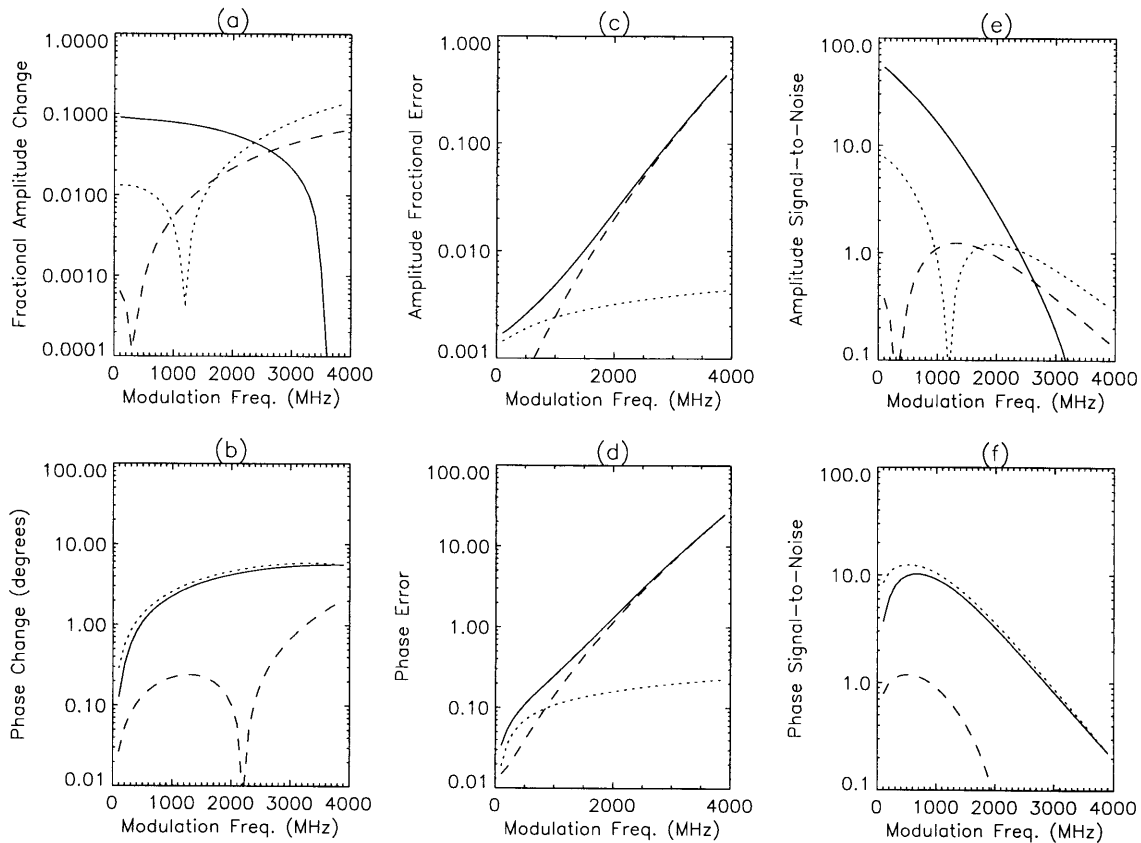
Absorbing Object

Fig. 12. Contributions of the monopole (solid curves), dipole (dotted curves), and quadrupole (dashed curves) moments of the scattered wave to (a) the amplitude, (b) the phase of the total wave are plotted versus the modulation frequency of the source. The source and the detector are separated by 6.0 cm with a 1.0-cm-diameter absorbing object centered between them. The optical properties of the object are given in Fig. 1. The noise in the amplitude and phase is given in (c) and (d), respectively. The dotted (dashed) curve corresponds to the positional (shot) noise. The solid curve is the combination of positional and shot noise. The signal-to-noise ratio for amplitude and phase is given in (e) and (f), respectively, for the monopole (solid curves), dipole (dotted curves), and quadrupole (dashed curves) moments.

B. Optimal Modulation Frequency

Comparing signal-to-noise ratios for different DPDW modulation frequencies, we can determine the optimal frequency for detecting and characterizing different objects. Figures 12(a) and 12(b) plot the change in the signal that is due to each moment relative to the incident wave [Eq. (8)] as a function of modulation frequency for an absorbing object. Although the magnitude of each moment is increasing with frequency, each moment's perturbation of the signal is not necessarily increasing because of interference between the moment and the incident wave. In fact, as is seen in Figs. 12(a) and 12(b), at 2200 MHz the quadrupole moment effects no phase shift and at 300 MHz the quadrupole moment effects no amplitude change. These nulls in general do not decrease the ability to characterize an object because a null in either the amplitude or the phase is compensated for by a large signal in the phase or the amplitude, respectively. On the other hand, the frequency at which these nulls occur depends on the characteristics of the object, and therefore they may

be exploited to improve object characterization. A similar idea has been suggested by Yao *et al.*[30]

The shot noise and positional error as functions of modulation frequency are plotted in Figs. 12(c) and 12(d). They exhibit an increase with modulation frequency, as expected. For the model system, the shot noise exceeds the positional noise at frequencies larger than 800 MHz. The crossover point for the amplitude noise occurs because the amplitude of the DPDW is decreasing exponentially as approximately the square root of the modulation frequency. Thus the fractional error that is due to shot noise is increasing exponentially. On the other hand, the fractional error that is due to positional uncertainty is increasing approximately with the square root of the modulation frequency. Because of the rapid increase in noise with modulation frequency, measurements at high modulation frequencies are undesirable. Likewise, measurements at low modulation frequencies are undesirable because of the small perturbations.

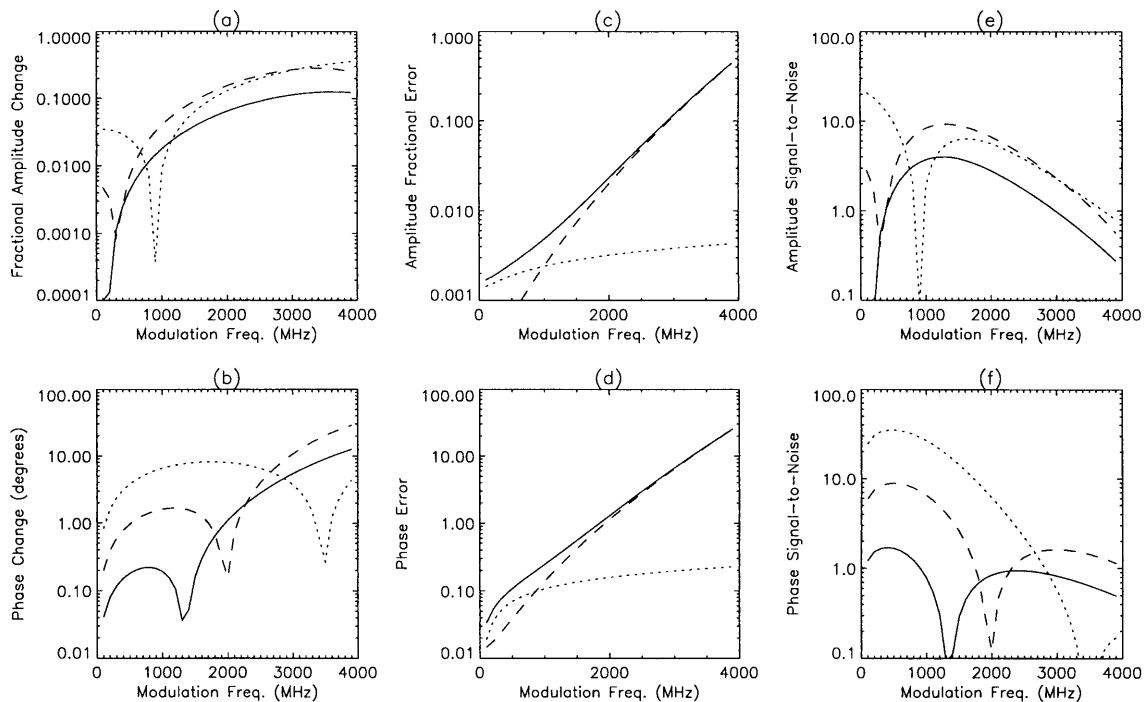To determine the optimal frequency for detection

Scattering Object

Fig. 13. Contributions of the monopole (solid curves), dipole (dotted curves), and quadrupole (dashed curves) moments of the scattered wave to (a) the amplitude, (b) the phase of the total wave are plotted versus the modulation frequency of the source. The source and the detector are separated by 6.0 cm with a 1.0-cm-diameter scattering object centered between them. The optical properties of the object are given in Fig. 1. The noise in the amplitude and phase is given in (c) and (d), respectively. The dotted (dashed) curve corresponds to the positional (shot) noise. The solid curve is the combination of positional and shot noise. The signal-to-noise ratio for amplitude and phase is given in (e) and (f), respectively, for the monopole (solid curves), dipole (dotted curves), and quadrupole (dashed curves) moments.

and characterization, we calculate the signal-to-noise ratio for the monopole, dipole, and quadrupole moments. These results are plotted in Figs. 12(e) and 12(f). The best signal-to-noise ratio is obtained near 0 MHz. Although the signal-to-noise ratio is smaller at higher modulation frequencies, it is possible to characterize accurately a 1.0-cm-diameter absorber at 2.0 GHz, because the monopole and the dipole perturbations still exceed the noise threshold.

Similar results were also obtained for the scattering objects (see Fig. 13). The main difference is that the best signal-to-noise ratio for scattering objects is obtained near 500 MHz.

Modulation frequencies between 0 and 500 MHz are appropriate when one considers the characterization of single objects embedded in otherwise homogeneous systems. If multiple objects are present and resolution becomes an issue, then measurements at higher modulation frequencies are desirable. By resolution, we mean the ability to distinguish signals that originate from different sources, e.g., the waves scattered from two distinct objects. Resolution improves with higher modulation frequencies because the DPDW wavelength decreases and we gain sensitivity to smaller length scales. The analytic techniques presented here permit us to determine the maximum modulation frequencies that provide useful information, but they do not provide a simple

framework for analyzing the resolving power of DPDW's. The reader is referred to Pattanayak[23] for a discussion on the resolving power of DPDW's.

C. Utilizing Spectral Information

It has been suggested that measurements of the amplitude and the phase of DPDW's at several modulation frequencies may be used to enhance sensitivity to the optical properties of a turbid medium.[3] We have investigated this possibility by comparing fractional uncertainties obtained with three different source–detector configurations. The three configurations are (1) modulation frequency held constant at 200 MHz, (2) modulation frequency scanned from 0 to 1000 MHz in steps of 200 MHz, and (3) modulation frequency scanned from 0 to 1000 MHz in steps of 100 MHz. In each of the three cases, the source was held fixed closest to the object and the detector was scanned from $x = -2.0$ to 2.0 cm in steps of 0.2 cm. Also, for each case the total number of independent measurements was kept constant at 210 measurements of amplitude and phase (i.e., at each position 10 measurements were made of amplitude and phase). In this way, any observed improvement in the characterization of the object can be attributed to spectral measurements rather than to an overall increase in the number of measurements. In case (1) this required making 10 measurements at 200 MHz
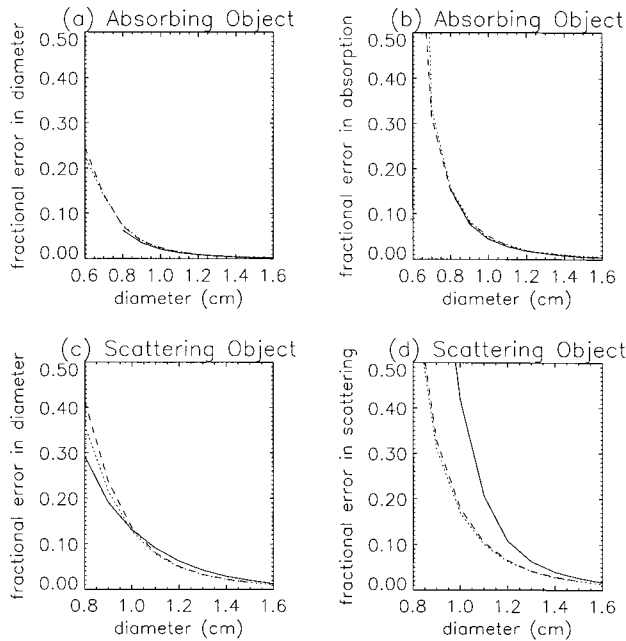
Fig. 14. Fractional uncertainties in (a) the diameter, (b) the absorption coefficient of an absorbing object are given versus the diameter of the object. In (c) and (d) the fractional uncertainties are given for a scattering object. Results are given for three different source detector configurations. In all configurations the source was held fixed closest to the object at $x = 0$ and the detector was scanned from $x = -2.0$ to 2.0 cm in steps of 0.2 cm. The solid curves correspond to a modulation frequency of 200 MHz, with 10 measurements made at each position. The dotted curves result from the modulation frequency scanned from 0 to 1000 MHz in steps of 200 MHz with two measurements at each position. Finally, the dashed curves correspond to one measurement at each position, with the frequency scanned from 0 to 1000 MHz in steps of 100 MHz. Note that the spectral measurements improve the characterization of the scattering coefficient of the scattering object but do not enhance the characterization of the absorbing object.

at each spatial position, whereas in case (2) two measurements were made at each frequency and each spatial position.

Figures 14(a) and 14(b) plot the fractional uncertainty in the diameter and the absorption coefficient of an absorbing object versus the diameter of the object for the three different source–detector configurations. No improvement is observed in the fractional uncertainty of the diameter or the absorption coefficient. On the other hand, for a scattering object a decrease in the fractional uncertainty of μ_s' is observed when measurements are made over a range of modulation frequencies [see Figs. 14(c) and 14(d)]. Spectral measurements thus enhance the characterization of scattering objects as well as provide a means of distinguishing scattering from absorbing objects.

D. Measurements at Multiple Optical Wavelengths

It is reasonable to expect that measurements at multiple optical wavelengths will improve our ability to characterize optical inhomogeneities. We show that this additional information does not improve our abil-
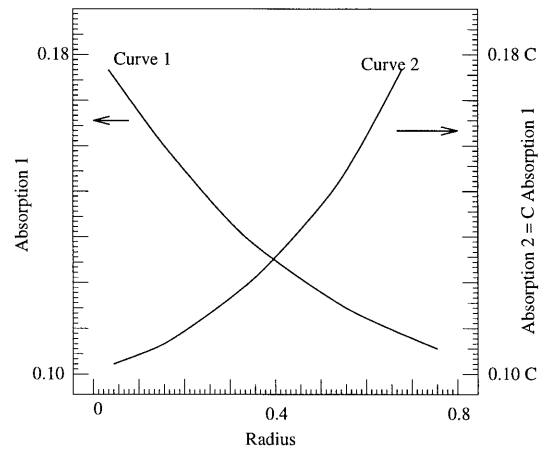

Fig. 15. Possible chi-squared valleys for a two-parameter fit for the object radius and the absorption coefficient at two different optical wavelengths.

ity to characterize the size and optical properties of inhomogeneities. Consider two sets of measurements made on the same sample: one at optical wavelength λ_1 and the other at optical wavelength λ_2. For each set we can independently characterize the size and the absorption coefficient of the object. Assuming that a common chromophore is the dominant absorber at the two optical wavelengths, then the size of the characterized absorber should be the same for each set. Thus, instead of having four unknowns $[a(\lambda_1), \mu_a(\lambda_1), a(\lambda_2),$ and $\mu_a(\lambda_2)]$, we have only three, and three parameters can be characterized more accurately than four.

This argument may sound reasonable, but we have to be careful. It is true that the uncertainties in the three parameters will be smaller than the uncertainties determined for the four parameters when the two data sets are characterized independently. However, will the uncertainties be any smaller than if all measurements were made at a single wavelength? Let us say that each data set has N measurements. In the first case we are using N measurements to get $a(\lambda_1)$ and $\mu_a(\lambda_1)$ and N measurements to get $a(\lambda_2)$ and $\mu_a(\lambda_2)$. In the second case we are using $2N$ measurements to determine a, $\mu_a(\lambda_1)$, and $\mu_a(\lambda_2)$. We would do better to use $2N$ measurements to find just two parameters, a and $\mu_a(\lambda_1)$.

What if we knew the absorption spectrum of the dominant chromophore at λ_1 and λ_2? In this case there would only be two unknowns because $\mu_a(\lambda_1)$ and $\mu_a(\lambda_2)$ would have a known proportionality C. This might lead to improved characterization. To see if this is possible we must consider the extended minima (or valleys) of the chi-squared surfaces for the different data sets. For a two dimensional chi-squared function, there is a valley that indicates the relation between systematic deviations in the two fitting parameters. The valley for fitting $a(\lambda_1)$ and $\mu_a(\lambda_1)$ may look like curve 1 in Fig. 15. This curve tells us what the deviation in a will be if we know the deviation in μ_a and vice versa. For repeated mea-
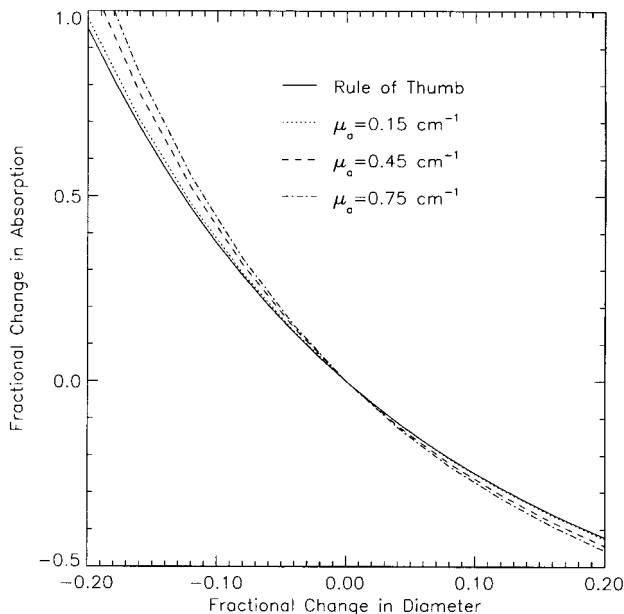
Fig. 16. Fractional deviation in the optical parameter versus the fractional deviation in the diameter. The optical parameter represents either the absorption coefficient or the scattering coefficient.

surements of the λ_1 data set, the determined a and μ_a values will always appear on curve 1. For λ_2 the valley may look like curve 2 in Fig. 15. Curve 1 and curve 2 intersect at the correct values for the object parameters. If we fit both data sets simultaneously with the constraint that $a(\lambda_2) = a(\lambda_1)$ and $\mu_a(\lambda_2) = C\mu_a(\lambda_1)$ then the fitting parameters will be drawn toward the intersection point of the two curves, decreasing the uncertainty. If the valleys nearly overlap, then the fitting parameters will not be strongly drawn toward the intersection point. Improved characterization is possible only if the different curves have significantly different slopes.

Valleys for three spherical objects with different absorption coefficients but the same radius are shown in Fig. 16. The dotted, dashed, and dashed–dotted curves were derived from simulations for 5-mm-diameter absorbers with absorption coefficients of 0.15, 0.45, and 0.75 cm^{-1}, respectively, relative to the background coefficient of 0.05 cm^{-1}. The other system parameters are indicated in Fig. 1. These valleys nearly overlap, and therefore we cannot use multiple optical wavelengths to improve object characterization. Even if the curves were more perpendicular, uncertainties associated with the dominant chromophore assumption would reduce any gains in object characterization.

7. Summary

The interaction between DPDW's and optical inhomogeneities provides a staightforward way of detecting and localizing inhomogeneities and a means for characterizing the size and optical properties of the inhomogeneity. If no noise were present in the measurements, then our ability to characterize these ob-

jects would be limited only by the validity of the model used for the analysis. Here, we have used an exact analytic model for the scattering of DPDW's from spherical inhomogeneities that is based on the diffusion approximation to the photon transport equation. This model is valid on length scales larger than the photon random-walk step, $1/\mu_s'$, which is ~1 mm for tissue. Unfortunately noise is always present, and, as we have seen, it diminishes our ability to characterize inhomogeneities.

Detecting and locating inhomogeneities is possible if the perturbation of the incident DPDW, the signal [see Eq. (8)], is greater than the noise threshold. The results presented here demonstrated that 3-mm-diameter objects are detectable for realistic parameters. For small absorbing objects the signal is dominated by the monopole moment, whereas for small scattering objects the signal is dominated by the dipole and the quadrupole moments. For transmission measurements, the strongest signal occurs when the object is directly between the source and the detector, and therefore a detectable object is easily located. Changing the modulation frequency does not greatly change the detectability of absorbing or scattering objects except at high frequencies at which the signal is obscured by shot noise (see Figs. 4, 6, 12, and 13). The detectability of objects with different optical properties embedded in the same system, as described in Fig. 1, can be determined from the leading-order form of the moments of the scattered DPDW [see Eqs. (2–4)]. For instance, the leading-order signal from a small absorbing object is proportional to $a^3\delta\mu_a$. This product, $a^3\delta\mu_a$, indicates how much larger a less absorbing object must be or how much smaller a more absorbing object can be in order for it to be still detectable. In particular, the product shows that the size of a detectable object scales as $\delta\mu_a^{-1/3}$. For example, given that an object with $\delta\mu_a = 0.1$ cm^{-1} is detectable if $a > 0.3$ cm, then an object with $\delta\mu_a = 0.05$ cm^{-1} is detectable if $a > 0.38$ mm.

Characterizing the size and optical properties of an object is not as straightforward because an indirect method is required, e.g., chi-squared fitting, to determine the parameters from measurements of the distorted DPDW. Furthermore, it is necessary for more than one moment of the scattered DPDW to perturb the signal by a detectable amount in order to distinguish the contributions from the object's size and optical properties. To determine the size and either the absorption or the scattering coefficient of an object, it is necessary for two moments to be detectable (i.e., two unknowns and two equations). Likewise, to determine three parameters accurately, it is necessary for at least three moments to be detectable. Because of these additional requirements, inhomogeneities cannot be accurately characterized unless they are 1 cm or larger in diameter for realistic parameters.

We have demonstrated that the measurement geometry can be optimized to characterize smaller objects. The only useful measurements are those for which the perturbation is detectable. Therefore, for

transmission through a slab geometry, it is best to make measurements with the source closest to the object and the detector scanned near the point of closest approach to the object or vice versa. We have also demonstrated that 0 MHz is the optimal frequency for detecting and characterizing absorbing objects. Scattering objects are best detected and characterized with modulation frequencies near 500 MHz. Characterization of scattering objects is further optimized by the use of measurements at several modulation frequencies.

Still smaller objects can be characterized if there is *a priori* knowledge of the size or optical properties of the object. For example, knowledge of the structural properties of the system obtained from a CAT scan or magnetic resonance imaging affords an accurate determination of the optical properties of tumors smaller than 1 cm. When the number of unknowns is reduced, accurate tumor characterization becomes feasible with the detection of fewer multipole moments. If we know the size of an absorbing or scattering object, then the optical contrast can be determined as long as the contribution from a single moment is detectable, likewise if the optical contrast is known and the size is sought. Thus, with prior knowledge, it is possible to characterize detectable objects accurately, i.e., objects of the order of 3 mm in diameter. Any uncertainty in the priorly known quantity will result in a systematic error in the determined quantity. For example, if the size of the object is measured by magnetic resonance imaging to be 5 mm and it is actually 4 mm, then the reconstructed absorption coefficient will be systematically reduced by 50%. The systematic deviation in the absorption (scattering) coefficient of an absorbing (scattering) object that is due to an incorrect previous determination of the size is described by the universal curve presented in Fig. 16. The solid curve derives from the $a^3 \delta\mu_a$ ($a^3 \delta\mu_s'$) dependence of the dominant contribution to the scattered wave from an absorbing (scattering) object and indicates that an overestimation of the size results in an underestimation of the optical parameter and vice versa. The dotted, dashed, and dashed–dotted curves were derived from simulations for 5-mm-diameter absorbers with absorption coefficients of 0.15, 0.45, and 0.75 cm^{-1}, respectively, relative to the background coefficient of 0.05 cm^{-1}. The observed deviation from the universal curve (solid curve) arises from the increased importance of higher-order multipole moments. This deviation is small, and thus the universal curve serves as a good rule of thumb. Note that this result is valid for objects of general shape when a^3 is replaced with the volume of the object.

The limits discussed here for detecting and characterizing optical inhomogeneities with DPDW's are based on ideal systems in which the noise is governed by shot noise and positional errors. The results should thus be viewed as a best case. In the clinical environment, other sources of noise are expected to exist that will further complicate the accurate characterization of optical inhomogeneities. For example, the intrinsic fluctuations of a biological sample about its average background value causes amplitude and phase shifts. If the intrinsic heterogeneity is not considered in imaging algorithms, then the corresponding signal fluctuations are essentially noise. Quantification of the intrinsic heterogeneity of different biological samples is necessary to determine if this type of noise is significant. Another source of systematic noise is the discrepancy between diffusion models and experiment. A discrepancy between models and experiment of 1% amplitude and a few degrees of phase is not uncommon, especially at higher modulation frequencies. Further investigation is required for determining the effect of this systematic noise on optical imaging.

References and Notes

1. B. Chance, ed., *Photon Migration in Tissues* (Plenum, New York, 1988).
2. A. Yodh and B. Chance, "Spectroscopy and imaging with diffusing light," Phys. Today **48**(3), 34–40 (1995).
3. B. J. Tromberg, L. O. Svaasand, T. Tsay, and R. C. Haskell, "Properties of photon density waves in multiple-scattering media," Appl. Opt. **32,** 607–616 (1993).
4. M. S. Patterson, B. Chance, and B. C. Wilson, "Time resolved reflectance and transmittance for the non-invasive measurement of tissue optical properties," Appl. Opt. **28,** 2331–2336 (1989).
5. E. M. Sevick, B. Chance, J. Leigh, S. Nioka, and M. Maris, "Quantitation of time- and frequency-resolved optical spectra for the determination of tissue oxygenation," Anal. Biochem. **195,** 330–351 (1991).
6. B. C. Wilson, E. M. Sevick, M. S. Patterson, and B. Chance, "Time-dependent optical spectroscopy and imaging for biomedical applications," Proc. IEEE **80,** 918–930 (1992).
7. J. B. Fishkin and E. Gratton, "Propagation of photon density waves in strongly scattering media containing an absorbing semi-infinite plane bounded by a straight edge," J. Opt. Soc. Am. A **10,** 127–140 (1993).
8. M. A. O'Leary, D. A. Boas, B. Chance, and A. G. Yodh, "Refraction of diffuse photon density waves," Phys. Rev. Lett. **69,** 2658–2661 (1992).
9. B. W. Pogue and M. S. Patterson, "Frequency-domain optical-absorption spectroscopy of finite tissue volumes using diffusion-theory," Phys. Med. Biol. **39,** 1157–1180 (1994).
10. F. F. Jobsis, "Noninvasive, infrared monitoring of cerebral and myocardial oxygen sufficiency and circulatory parameters," Science **198,** 1264–1267 (1977).

11. S. J. Matcher, C. E. Elwell, C. E. Cooper, M. Cope, and D. T. Delpy, "Performance comparison of several published tissue near-infrared spectroscopy algorithms," Anal. Biochem. **227,** 54–68 (1995).

12. H. Liu, D. A. Boas, Y. Zhang, A. G. Yodh, and B. Chance, "Determination of optical properties and blood oxygenation using continuous NIR light," Phys. Med. Biol. **40,** 1983–1993 (1995).

13. V. G. Peters, D. R. Wyman, M. S. Patterson, and G. L. Frank, "Optical properties of normal and diseased human breast tissues in the visible and near infrared," Phys. Med. Biol. **35,** 1317–1334 (1990).

14. A table of published optical properties compiled by L. Wang and S. Jacques is available from ftp://laser.mda.uth.tmc.edu/pub/tissue/Cheong1990.msw or ftp://laser.mda.uth.tmc.edu/pub/tissue/Cheong1990.ps.

15. D. A. Boas, M. A. O'Leary, B. Chance, and A. G. Yodh, "Scattering and wavelength transduction of diffuse photon density waves," Phys. Rev. E **47,** R2999–R3002 (1993).

16. D. A. Boas, M. A. O'Leary, B. Chance, and A. G. Yodh, "Scattering of diffuse photon density waves by spherical inhomogeneties within turbid media: analytic solution and applications," Proc. Natl. Acad. Sci. USA **91,** 4887–4891 (1994).

17. P. N. den Outer, T. M. Nieuwenhuizen, and A. Lagendijk, "Location of objects in multiple-scattering media," J. Opt. Soc. Am. A **10,** 1209–1218 (1993).

18. S. Feng, F. Zeng, and B. Chance, "Photon migration in the presence of a single defect: a perturbation analysis," Appl. Opt. **34,** 3826–3837 (1995).

19. J. M. Schmitt, A. Knuttel, and J. R. Knutson, "Interference of diffusive light waves," J. Opt. Soc. Am. A **9,** 1832–1843 (1992).

20. B. Chance, K. Kang, L. He, J. Weng, and E. Sevick, "Highly sensitive object location in tissue models with linear in-phase and anti-phase multi-element optical arrays in one and two dimensions," Proc. Natl. Acad. Sci. USA **90,** 3423–3427 (1993).

21. J. Maier and E. Gratton, "Frequency domain methods in optical tomography: Detection of localized absorbers and a backscattering reconstruction scheme," in *Photon Migration and Imaging in Random Media and Tissues*, B. Chance and R. R. Alfano, eds., Proc. SPIE **1888,** 440–451 (1993).

22. A. Knuttle, J. M. Schmitt, and J. R. Knutson, "Spatial localization of absorbing bodies by interfering diffusive photon density waves," Appl. Opt. **32,** 381–389 (1993).

23. D. Pattanayuk, "Resolution of optical images formed by diffusive waves in highly scattering media," General Electric Consumer Research and Development Rep. (General Electric, Schenectady, N.Y., 1992).

24. J. A. Moon and J. Reintjes, "Image resolution by use of multiply scattered light," Opt. Lett. **19,** 521–523 (1994).

25. A. H. Gandjbakhche, R. Nossal, and R. F. Bonner, "Resolution limits for optical transillumination of abnormalities deeply embedded in tissues," Med. Phys. **21,** 185–191 (1994).

26. M. Essenpreis, C. E. Elwell, M. Cope, P. van der Zee, S. R. Arridge, and D. T. Delpy, "Spectral dependence of temporal point spread functions in human tissues," Appl. Opt. **32,** 418–425 (1993).

27. D. G. Papaioannou, G. W. 't Hooft, J. J. M. Baselmans, and M. J. C. van Gemert, "Image quality in time-resolved transillumination of highly scattering media," Appl. Opt. **34,** 6144–6157 (1995).

28. D. A. Boas, L. E. Campbell, and A. G. Yodh, "Scattering and imaging with diffusing temporal field correlation," Phys. Rev. Lett. **75,** 1855–1858 (1995).

29. P. R. Bevington, *Data Reduction and Error Analysis for the Physical Sciences* (McGraw-Hill, New York, 1969).

30. Y. Yao, Y. Wang, R. L. Barbour, H. L. Graber, and J. Chang, "Scattering characteristics of photon density waves from an object embedded in a spherically two-layer turbid medium," in *Optical Tomography, Photon Migration, and Spectroscopy of Tissue and Model Media: Theory, Human Studies, and Instrumentation*, B. Chance and R. R. Alfano, eds., Proc. SPIE **2389,** 291–303 (1995).